

Preparation of 3D Printable HAp-based Composite Powder for Binder Jetting Process

Fahimeh Dini

Iran University of Science and Technology

Seyed Amir Ghaffari (✉ amirghaffari@iust.ac.ir)

Iran University of Science and Technology <https://orcid.org/0000-0003-2444-7061>

Jafar Javadpour

Iran University of Science and Technology

Hamid Reza Rezaie

Iran University of Science and Technology

Research Article

Keywords: Additive Manufacturing, Binder Jet, Hydroxyapatite, 3D printable powder

Posted Date: September 17th, 2020

DOI: <https://doi.org/10.21203/rs.3.rs-76994/v1>

License: © ⓘ This work is licensed under a Creative Commons Attribution 4.0 International License.

[Read Full License](#)

Abstract

The purpose of this study was to prepare a 3D printable powder composed of hydroxyapatite and biocompatible polymers such as chitosan, dextrin, and polyvinylpyrrolidone for the binder jetting process. The relationship between powder properties such as flowability and particle size distribution, as well as printing quality were investigated in the binder jetting process. For this purpose, 3D printable powder and an appropriate solvent were designed and demonstrated by hydroxyapatite and water-soluble polymers such as carboxymethyl chitosan, dextrin, and PVP. Results showed that a combination of 60%wt. hydroxyapatite, 28%wt. carboxymethyl chitosan, 10% wt. dextrin, and 2% wt. PVP, with controlled particle size distribution according to the Dinger-Funk equation led to the best print quality. Finally, flash dipping of the 3D printed parts in chitosan solution resulted in increases of compressive and Young's modulus from 1.3 and 10 MPa to 7.4 and 125 MPa, respectively.

1. Introduction

Every year, millions of patients suffer from bone tissue loss due to pathological events such as trauma, disease, or surgery. Consequently, bone reconstruction procedures are widely implemented using autografts or allografts to improve bone healing in a critically sized defect. However, these bone scaffolds and grafts suffer from many limitations, originated from the traditional shaping method, which makes synthetic alternatives an attractive option. Calcium phosphate (CaP) ceramics are superior and promising candidates to repair the bone defect since they decrease the problems of the rejection reaction and donor scarcity. Furthermore, they have a long history of synthetic bone replacement due to their chemical similarity to bone minerals [1–3]. Hydroxyapatite ($\text{Ca}_{10}(\text{PO}_4)_3\text{OH}$) is widely used due to the excellent physiological and environmental biocompatibility, as well as compatibility with synthetic and natural polymers such as polysaccharides and proteins (e.g. collagen). Consequently, a combination of HAp and biocompatible polymers creates a functional biomaterial for medical and veterinary applications [4].

The excellent application potential of additive manufacturing (AM) technology, more commonly known as 3D printing, in bone tissue engineering is widely noticed in previous works [5–12]. Among AM techniques, only direct extrusion 3D printing and binder jetting 3D printing can fabricate the scaffolds at low temperatures [13]. Thus, these techniques are highly beneficial since they provide the potential to create composites with synthetic or biological polymers [1]. Binder jetting (BJT) is an AM technology suitable for the production of high complexity 3D components using ceramic or metal precursor powders, with the potential for various applications, wherein a roller mechanism spreads the powder material, forming a bed, and then an inkjet print head moves in the XY plane of the machine selectively jetting the binder agent [14]. In the binder jetting processes, the binder can be applied in three different routes [15]. In the first one, called binder jetting in place, binder material is diluted in an appropriate solvent, and then jetted onto the powder bed. The second route, called binder pre-mixing, is to mix binder uniformly and ceramic powder together, followed by milling and mixing of the mixture [16, 17]. In the third way, called binder pre-coating, the ceramic powder and binder particles are dissolved in the binder solvent to obtain a

mixture slurry. Then, the slurry can be dried or spray dried, milled, and sieved to obtain a binder-coated ceramic powder [18–20].

Numerous attempts have been made to fabricate hydroxyapatite bioceramic bone scaffolds using the binder jetting technology, and many remarkable achievements have been obtained in the field of biomedical engineering [21–32].

The major challenge in scaffold fabrication via BJT is to select the type and amount of binder, which leads to high green strength, and the method of binder added to the powder stock [33]. Unfortunately, despite the importance of the powder properties, which profoundly influences printing accuracy, there has to date been a limited number of practical scaffold 3D printing works showing the relation between the powder properties and the printing outcome [3].

As a controversial subject, the powder size and shape is a crucial factor determining the quality of the printed components by influencing the surface roughness, flowability, and packing density of powder bed, which are essential parameters for the layer-based additive manufacturing techniques. The challenge is to select an optimum particle size; a small particle size may increase the packing density. However, it quickly causes the formation of large and stable agglomerates, which leads to a decrease in flowability. Although large particles have good flowability, they cause lower packing density and a rough surface [3, 13]. It was suggested in previous works that the multi-modal powders, by a mixture of fine and coarse powders in a particular ratio, lead to the optimization of the challenging parameters. This is because fine powders fill the gaps among coarse powders, resulting in increased overall packing density and improved mechanical properties of the printed part [34, 35].

The principles mentioned above suggest that a complicated relationship must exist between powder properties and the final additive manufactured scaffold properties. Due to the given theoretical and technical limitations, this study aims to prepare a 3D printable powder using HAp/biocompatible polymer composite for the BJT process. The relation between relevant powder properties, printability, and final properties of 3D printed parts was investigated here.

2. Materials And Methods

2.1. Powder preparation

Hydroxyapatite (Merck, Germany, CAS No. 1306-06-5, 100% purity), chitosan (CMS) (Sigma-Aldrich, Germany, 100% purity), dextrin (Bonfozhan Kimia, Iran, 100% purity), and polyvinylpyrrolidone (PVP) (Rahavard Tamin, Iran, 100% purity) were used as the primary materials. Firstly, chitosan was transformed into Carboxymethyl Chitosan (CMCTS) through a synthesis process to obtain a water-soluble composition according to a previous report by Lu et al [36]. Considering that HAp 60wt.%: Chitosan40wt.% is the composition as an artificial bone, different arrangements of HAp and polymer binders were mixed in aqueous solution with 1:4 powder to water ratio according to Table 1. The slurries

were dried at 60 °C for 24 hours, ground, and passed through different sieves to adjust particle size distribution.

Table 1
Characteristics of powdered batches

powder	HAP%wt.	CMCTS%wt.	PVP%wt.	Dextrin%wt.	Ball milling time (hour)	Passing the sieve (sieve mesh)
P1	60	40	0	0	12	80
						120
P2	60	38	2	0	12	80
						120
P3	60	28	2	10	12	80
						120
P4	60	28	2	10	12	140
						170
						230
						325
						400
P5	60	28	2	10	72	140
						170
						230
						325
						400

2.2. Powder characterization

The particle size distribution of the powders was designed according to the selected sieves (Table 1). The morphology of prepared composite powders was investigated by scanning electron microscopy (SEM) (TESCAN, Czech Republic).

The standardized test methods were used to measure the apparent density and tap density of the prepared powders [37, 38]. In previous reports [35, 39, 40], the Hausner rate was defined as a quantitative number showing the flowability of printable powders, which is defined as the ratio of the tapped density to the apparent density.

2.3. 3D Printing of samples

The printability of prepared powders was evaluated by 3D printing of hexagonal shape with a 20 mm diameter and a 5 mm height using a homemade BJT machine, working with a piezoelectric printing head. 3D printing parameters of the device were fixed at 200 μm layer thickness, powder roller spreading speed of 50 cm/sec, layer printing intervals of 2 secs, printing speed of 1 cm^2/sec , and binder saturation of 50%. Table 2 shows the composition of the water based binder. The best 3D printable powder was selected among the samples having the optimum values of spread and flowability, binder adhesion, and solution to binder ratio. The final printed parts had high dimension accuracy, appropriate density, and desired mechanical strength of a biocomposite.

Table 2
Composition of binding liquid

Content (wt. %)
Deionized water 70
Glycerin 20 Medical grade
Isopropyl alcohol 10 Medical grade

2.4. Sample characterization

Infrared spectroscopy analysis (Shimadzu S 8400, Japan) was utilized to examine likely changes in polymers structure. Density measurement of printed samples was carried out according to the C373-88 ASTM standard [41, 42].

The compressive strength of samples was measured by a universal testing machine (SANTAM SAF-50, Iran) with a uniaxial force rate of 0.5 mm/min. Mechanical test samples were 3Dprinted in the form of a cylinder, with 5 mm diameter and 10 mm height, according to the ISO5833 standard. Post-print processing operations included flash dipping of the 3D printed samples in a 0.5 wt.% chitosan solution, followed by drying at 40 °C for 24 hours, which was carried out to increase the strength of printed samples.

3. Results And Discussion

3.1. Characterization of powdered batches

Figure 1 represents the SEM image of hydroxyapatite and composite powders. Given the surface morphology and particle size change, it can be concluded that the HAp particles were mixed by the CMCTS, dextrin, and PVP to form new composite powder with larger granules, in that smoother surface can be an evidence for the presence of polymers.

According to a report provided by Inzana et al. [1], two sieves 80 (177 μm) and 120 (125 μm) were used for powders P1-P3 to remove large and fine particles, respectively, to attain high dimensional accuracy in the printed parts and prevent the agglomeration of fine particles. Considering a report by Bai et al. [35], remained powders under 80 and 120 mesh sieves were then mixed by a ratio of 30:70.

The Dinger-Funk equation was applied as an alternative approach for particle size distribution optimization of P4 and P5 powders assuming that all possible particle sizes were present in the final distribution.

$$\text{Eq. 1 } \frac{CPFT}{100} = \frac{D^n - D_s^n}{D_i^n - D_s^n}$$

In Eq. 1, CPFT is the cumulative percent of particles finer than a given particle size D , D_i is the size of the largest particle, D_s is the size of the smallest particle and n is Dinger-Funk particle size distribution modulus. According to this Equation, considering a constant printing layer height thickness of the print layer in this study (200 μm) and a report presented by Spierings et al. [43], the highest powder flowability and layer packing density are obtained when the D_{90} of powder is smaller than layer thickness (200 μm); moreover, D_{10} should not be lower than 5 μm . The sizes of the smallest and largest particle were considered 5 and 105 μm , respectively. In order to obtain the highest packing density, a n power of 0.37 was considered in Eq. 1.

Table 3
Characterization of prepared powdered batches according to Dinger-Funk equation

powder	D_{90} (μm)	D_{50} (μm)	D_{10} (μm)	D_{50} / D_{10}	D_{90} / D_{10}	PSD width
P4, P5	89	37	11	3.36	8.09	2.10

Table 3 describes the characterization of optimized powders via the Dinger-Funk equation. The particle size distribution width was defined as $(D_{90}-D_{10})/D_{50}$. The higher the numerical value obtained for this parameter, the broader the particle size distribution, and the smaller the numerical value, the narrower the particle size distribution [44]. In a study performed by Karapatiz [39], the criteria for proper particle size distribution were reported as follows:

1) $D_{90} < t$ Layer

2) $D50 / D10 \geq 10$

3) $D90 / D10 \leq 19$

However, the value for $D50/D10$, calculated according to the Dinger-Funk equation (Table 2), is smaller than 10 and did not pass the criteria expressed by Karapatiz; this condition was ignored in this study. However, it is within the range reported by Spiering et al. [43] Since the thickness of the printed layers is 200 μm in this process, the condition of Expression 1 was satisfied in both samples.

Table 4
Apparent density, tap density and Hausner ratio of prepared powders

powder	Apparent density (gr/cm^3)	Tapped density (gr/cm^3)	Hausner ratio
P1	1.256	1.535	1.22
P2	0.760	0.989	1.30
P3	1.08	1.36	1.25
P4	1.043	1.284	1.23
P5	1.06	1.34	1.26

Table 4 represents the tap and apparent densities of P1-P5 powders, and the Hausner ratio. An increase in the PVP percentage in P2 powder led to decreased apparent and tap densities, followed by the rise of the Hausner ratio. This effect is attributed to declined HAp granule sizes due to the dispersing behavior of PVP [45, 46], and consequently, an increase in the van der Waals force followed by diminishing the filling properties of the powder. The effect of particle size and density reduction by PVP was somewhat reduced in powders P3-P5 due to the use of dextrin along with CMCTS and PVP.

The lowest and the highest Hausner ratios were 1.22 and 1.3 for P2 and P3 powders, respectively (Table 3). A comparison of P1 and P2 reveals that adding PVP to P2 results in finer granules. PVP has both hydrophilic and hydrophobic groups and functions as a surfactant resulting in particle size reduction and an increase in the van der Waals force, leading to the formation of low-flow agglomerates [47]. Well-flowing powders can move quickly and, by occupying less space and reducing the cavities between the powder particles, lead to an increase in density. Low-flow powders also reduce density due to their inability to move. From what deduced before, it can be concluded that the P1 powder with the lowest Hausner ratio has the best flowability.

In order to evaluate printability, P1-P5 powders were printed as a 3D hexagonal shape model, named A1-A5, respectively. Layer shifting was observed during 3D printing of A1 sample with the lowest Hausner rate, due to a high flow rate in this sample, and consequently, the fast distribution of the layers by the

roller. Moreover, this sample showed high shrinkage, and hence, the edges of the model have a protruding protuberance on the surface. The high dissolution rate of CMTC in water and its fast reaction with HAp powder caused rapid bonding of the particles to each other and, consequently, occurring different shrinkage of outer and inner layers.

Due to the presence of PVP in the P2 sample, bonding between powder particles is improved in one layer compared to powder P1. In fact, due to the property of surface film formation, this polymer was used as the third component to eliminate layer shifting and edge protuberance in sample A1. The PVP powder particles swell as they moisten and form a surface film following the polymer chains. This swelling is low at low molecular weights and very high at high molecular weights. The higher the molecular weight of the PVP used, the higher its ability and the more particles form the film will be [48]. Adding the PVP eliminated layer shifting and edge protuberance, but it lowered the green strength.

Dextrin was added to P3 powder to increase the green strength of the printed sample. The green strength of the A3 sample increased due to the improvement of bonding between the particles. According to a patent by Liu. et al. [49], the presence of at least one carbohydrate as an active binding agent is required in the binder used in the BJT process.

By obtaining good green strength after reaching an ideal composition, the effect of particle size adjustment in P4 revealed good flowability and packing density of the A4 sample. An increase in the slurry mixing time in the P5 sample improved the bonding of powder particles and resulted in the highest green strength in printed samples (Fig. 2).

3.2. Characterization of composite components

Cylindrical shape samples with 5 mm diameter and 10 mm height were 3d printed from P5 powder, as revealed in Fig. 3.

SEM images (Fig. 4a and 4b) show the printed sample before and after flash dipping in the chitosan solution, respectively. Immersion in the chitosan solution decreased the porosity in the sample due to partial closure of some surface [50].

Figure 4a clearly shows that large and small pores remained from incomplete binder penetration in some parts of the powder bed during the 3d printing [51]. In the powder-bed AM method, particles with different sizes become separated by moving powder; the coarser particles form a coarse particle front at the top of the powder layer due to the better flow, and the fine particles fall to the bottom of the layer. Consequently, the non-filling of the voids occurs between the larger particles by the fine particles and eventually causes the creation of the cavities. These results are consistent with a report by Jacob et al. [52] who found that finer particles moved away from larger particles by accumulating in the lower layers of the powder bed.

The porosity of the printed parts was measured by the Archimedes method. Printed parts without any processing operation showed average and maximum porosity levels of 42% and 45.31%, respectively, ranging between 40 and 45%. The flash dipping of the printed sample in the chitosan solution reduced the porosity. The porosity of these samples was in the range of 30–36%, with an average of 34% and a maximum of 36.42%. Mean apparent green density and bulk density of respectively 1.74 g/cm³ and 1.01 g/cm³ were calculated for A5, and 1.86 g/cm³ and 1.18 g/cm³ for A5-D samples for A5. The increase in both densities in the A5-D samples can be attributed to the decreased porosity percentage, and to the chitosan introduced artificially into the printed sample structure. The significant differences in the densities of both groups can be attributed to the presence of closed porosities and a lack of a good correlation between the pores.

In the CMCTS spectra, the peak at 1612 cm⁻¹ belongs to the carboxyl group (-COOH) added to the polymer. Since the carboxyl group usually appears at 1730 cm⁻¹, its displacement in the corresponding spectrum is due to the conversion of the -COOH group to the carboxylic acid salt (-COONa). The peak at about 1429 cm⁻¹ belongs to the -CH₂COOH group. In the CTS spectrum, the peaks in the wavenumbers 1076 cm⁻¹ and 1024 cm⁻¹ indicate the C-O bond stretch. In the CMCTS spectra, however, the peak at 1139 cm⁻¹ is related to the C-O bond. The peak at 1056 cm⁻¹ also represents the primary hydroxyl group (-CH₂-OH), which is substituted with the carboxymethyl group. By comparing the wavenumbers for the O-H bond, it can be seen that this bond has shifted to a greater extent for the CMCTS. Peaks at 3600 – 3400 cm⁻¹ in both A5 and A5-D spectra are related to the tensile vibrations of O-H bonds (hydroxyl group) in hydroxyapatite. The peaks at 3420 cm⁻¹ and 3409 cm⁻¹ in both spectra can be attributed to the O-H stretching vibrations in the CMCTS, dextrin, and PVP. Peaks in the range of 2700 – 2000 cm⁻¹ in both samples belong to the HPO₄²⁻ groups in hydroxyapatite. Due to the use of acetic acid for chitosan dissolution, the shoulder created at 1712 cm⁻¹ in sample A5-D indicates the presence of free acetic acid. Moreover, since this acid is composed of only one -COOH group, it can branch out the chitosan and thereby increase its mechanical properties [53]. Peaks appearing in the range of 1000 – 100 cm⁻¹ in the spectra of both samples can also be attributed to the different bending states of the P-O bond in the PO₄⁻³ group of hydroxyapatite.

Figure 6. shows the stress-strain behavior of samples A5 and A5-D. As can be seen, the strength is increased by using flash dipping in the chitosan solution.

Compressive strength and modulus of elasticity in the A5 specimen are 1.3 and 10 MPa, respectively. These values for the flash dipped sample, A5-D, increased to 7.4 and 125 MPa, respectively, which can be attributed to the amino groups of chitosan protonated in the acetic acid solution. Since nitrogen atom in the amine group (NH³⁺) is more electronegative than hydrogen, nitrogen becomes negatively charged. On

the other hand, nitrogen in the amine group has two free electrons in its valence layer. Due to the Ca^{+2} ion in hydroxyapatite, nitrogen leads to a covalent bond by sharing two valence electrons with calcium. By artificial incorporation of chitosan into the flash dipped sample structure, the covalent bond between the chitosan amine group and the hydroxyapatite metal ion results in increased compressive strength and modulus of elasticity in this sample [54]. On the other hand, as noted in the porosity measurement section, there is an 8% reduction in the porosity of the A5-D sample compared to the A5 sample, which improves the mechanical properties.

Chavana et al. [55] reported a maximum compressive strength of 16 MPa and 30% porosity for a composite including 40% hydroxyapatite, 60% chitosan, and lactic acid printed using the BJT process and immersed in 40% wt. Lactic acid solution. By comparing the results of this study with previous reports, the strength obtained for the A5-D specimen showed acceptable results regarding the amount of hydroxyapatite.

4. Conclusion

The best composition among the powders was P5 with 60% HAp, 28% CMTc, 10% dextrin, 2% PVP with a particle size width of 2.10, and a Hausner ratio of 1.26 compared with the other powders.

Both the apparent and tap densities can be increased by optimizing the particle size distribution using the Dinger-Funk equation; in addition, it results in suitable powder flowability and optimum print quality.

Flash dipping in chitosan solution improves the mechanical properties of printed samples and increases their compressive strength from 1.3 to 7.4 MPa. The composite sample printed in this research has a maximum of 42% porosity, which decreases to 36% by flash dipping in chitosan solution.

Declarations

Acknowledgements

This research was partially supported by the Vice-Chancellery for Research and Technology, Iran University of Science and Technology. We thank our colleagues from the School of Materials and Metallurgy Engineering, who provided insight and expertise that greatly assisted the research.

References

- [1] Inzana JA, Olvera D, Fuller SM, et al. 3D printing of composite calcium phosphate and collagen scaffolds for bone regeneration. *Biomaterials* 2014, 35: 4026–4034.
- [2] Sun C, Tian X, Wang L. Effect of Particle Size Gradation on the Performance of Glass-Ceramic 3D Printing Process. *Ceram Int* 2016, 43: 578–584.
- [3] Butscher A, Böhner M, Roth C, et al. Printability of calcium phosphate powders for three-dimensional printing of tissue engineering scaffolds. *Acta Biomater* 2012, 8: 373–385.

- [4] Pighinelli L, Kucharska M. Chitosan-hydroxyapatite composites. *Carbohydr Polym* 2013, 93: 256–262.
- [5] Madrid APM, Vrech SM, Sanchez MA, et al. Advances in additive manufacturing for bone tissue engineering scaffolds. *Mater Sci Eng C* 2019, 100: 631–644.
- [6] Kumar A, Mandal S, Barui S, et al. Low temperature additive manufacturing of three dimensional scaffolds for bone-tissue engineering applications: Processing related challenges and property assessment. *Mater Sci Eng R Reports* 2016, 103: 1–39.
- [7] Castilho M, Gouveia B, Pires I, et al. The role of shell/core saturation level on the accuracy and mechanical characteristics of porous calcium phosphate models produced by 3Dprinting. *Rapid Prototyp J* 2015, 21: 43–55.
- [8] Khalyfa A, Vogt S, Weisser J, et al. Development of a new calcium phosphate powder-binder system for the 3D printing of patient specific implants. *J Mater Sci Mater Med* 2007, 18: 909–916.
- [9] Lee M, Dunn JCY, Wu BM. Scaffold fabrication by indirect three-dimensional printing. *Biomaterials* 2005, 26: 4281–4289.
- [10] Leukers B, Gulkan H, Irsen S, et al. Biocompatibility of ceramic scaffolds for bone replacement made by 3D printing. *Materwiss Werksttech* 2005, 36: 781–787.
- [11] Seyed Shirazi SF, Gharekhani S, Mehrali M, et al. A review on powder-based additive manufacturing for tissue engineering: selective laser sintering and inkjet 3D printing. *Sci Technol Adv Mater* 2015, 16: 033502.
- [12] Trombetta R, Inzana JA, Schwarz EM, et al. 3D Printing of Calcium Phosphate Ceramics for Bone Tissue Engineering and Drug Delivery. *Ann Biomed Eng* 2017, 45: 23–44.
- [13] Chai W, Wei Q, Yang M, et al. The printability of three water based polymeric binders and their effects on the properties of 3D printed hydroxyapatite bone scaffold. *Ceram Int* 2019, 46: 6663–6671.
- [14] Díaz-Moreno CA, Lin Y, Hurtado-Macias A, et al. Binder jetting additive manufacturing of aluminum nitride components. *Ceram Int* 2019, 45: 13620–13627.
- [15] Du W, Ren X, Ma C, et al. Binder Jetting Additive Manufacturing of Ceramics: A Literature Review. *Int Mech Eng Congr* 2018.
- [16] Fu Z, Schlier L, Travitzky N et al. Three-dimensional printing of SiSiC lattice truss structures. *Mater Sci Eng A* 2013, 560: 851–856.
- [17] Yin X, Travitzky N, Greil P. Near-Net-Shape Fabrication of Ti_3AlC_2 -Based Composites. *Int J Appl Ceram Technol* 2007, 190: 184–190.

- [18] Nan B, Yin X, Zhang L, et al. Three-Dimensional Printing of Ti_3SiC_2 -Based Ceramics. *J Am Ceram Soc* 2011, 94: 969–972.
- [19] Melcher R, Travitzky N, Zollfrank C, et al. 3D printing of $Al_2O_3/Cu-O$ interpenetrating phase composite. *J Mater Sci* 2011, 46: 1203–1210.
- [20] Winkel A, Meszaros R, Reinsch S, et al. Sintering of 3D-Printed Glass/HAp Composites. *J Am Ceram Soc* 2012, 95: 3387–3393.
- [21] Suwanprateeb J, Sanngam R, Panyathanmaporn T. Influence of raw powder preparation routes on properties of hydroxyapatite fabricated by 3D printing technique. *Mater Sci Eng C* 2010, 30: 610–617.
- [22] Suwanprateeb J, Sanngam R, Suwanpreuk W. Fabrication of bioactive hydroxyapatite / bis-GMA based composite via three dimensional printing. *J Mater Sci Mater Med* 2008, 19: 2637–2645.
- [23] Suwanprateeb J, Thammarakcharoen F, Hobang N. Enhancement of mechanical properties of 3D printed hydroxyapatite by combined low and high molecular weight polycaprolactone sequential infiltration. *J Mater Sci Mater Med* 2016, 27: 171.
- [24] Li X, Yuan Y, Liu L, et al. 3D printing of hydroxyapatite / tricalcium phosphate scaffold with hierarchical porous structure for bone regeneration. *Bio-Design Manuf* 2019, 3: 15–29.
- [25] Kumar A, Nune KC, Misra RDK. Biological functionality of extracellular matrix-ornamented three-dimensional printed hydroxyapatite scaffolds. *J Biomed Mater Res Part A* 2016, 104: 1343–1351.
- [26] Goncalves EM, Oliveira FJ, Silva RF, et al. Three-dimensional printed PCL-hydroxyapatite scaffolds filled with CNTs for bone cell growth stimulation. *J Biomed Mater Res Part B* 2015, 104: 1210–9.
- [27] Suwanprateeb J, Sanngam R, Suvannapruk W, et al. Mechanical and in vitro performance of apatite – wollastonite glass ceramic reinforced hydroxyapatite composite fabricated by 3D-printing. *J Mater Sci Mater Med* 2009, 20: 1281–1289.
- [28] Spath S, Drescher P, Seitz H. Impact of Particle Size of Ceramic Granule Blends on Mechanical Strength and Porosity of 3D Printed Scaffolds. *Materials (Basel)* 2015, 8: 4720–4732.
- [29] Zhang H, Mao X, Du Z, et al. Three dimensional printed macroporous polylactic acid / hydroxyapatite composite scaffolds for promoting bone formation in a critical-size rat calvarial defect model. *Sci Technol Adv Mater* 2016, 17: 136–148.
- [30] Wang YE, Li XP, Li CC, et al. Binder droplet impact mechanism on a hydroxyapatite microsphere surface in 3D printing of bone scaffolds. *J Mater Sci* 2015, 50: 5014–5023.
- [31] Cox SC, Thornby JA, Gibbons GJ, et al. 3D printing of porous hydroxyapatite scaffolds intended for use in bone tissue engineering applications. *Mater Sci Eng C* 2015, 47: 237–247.

- [32] Suwanprateeb J, Thammarakcharoen F, Wasoontararat K, et al. Influence of printing parameters on the transformation efficiency of 3D-printed plaster of paris to hydroxyapatite and its properties. *Rapid Prototyp J* 2012, 18: 490–499.
- [33] Vasireddi R, Basu B. Conceptual design of three-dimensional scaffolds of powder-based materials for bone tissue engineering applications. *Rapid Prototyp J* 2015, 21: 716–724.
- [34] Lv X, Ye F, Cheng L, et al. Binder jetting of ceramics: Powders, binders, printing parameters, equipment, and post-treatment, *Ceram Int* 2019, 45: 12609–12624.
- [35] Bai Y, Wagner G, Williams CB. Effect of Particle Size Distribution on Powder Packing and Sintering in Binder Jetting Additive Manufacturing of Metals. *J Manuf Sci Eng* 2017, 139: 081019.
- [36] Luo Y, Teng Z, Wang X, et al. Development of carboxymethyl chitosan hydrogel beads in alcohol-aqueous binary solvent for nutrient delivery applications. *Food Hydrocoll* 2013, 31: 332–339.
- [37] DIN EN 725-8. Advanced technical ceramics – methods of test for ceramic powders – part 8: determination of tapped bulk density. 2006.
- [38] DIN EN 725-9. Advanced technical ceramics – methods of test for ceramic powders – part 9: determination of untapped bulk density. 2006.
- [39] Spierings AB, Levy G. Comparison of Density of Stainless Steel 316L parts produced with Selective Laser Melting using Different Powder Grades. *SFF Symp* 2009, 1–12.
- [40] Zocca A, Gomes CM, Mühler T, et al. Powder-bed stabilization for powder-based additive manufacturing. *Adv Mech Eng* 2014, 6: 491581.
- [41] Castilho M, Rodrigues J, Pires I, et al. Fabrication of individual alginate-TCP scaffolds for bone tissue engineering by means of powder printing. *Biofabrication* 2015, 7: 015004.
- [42] Richerson D. *Modern Ceramic Engineering: Properties, Processing, and Use in Design*. CRC Press, 3rd edition, 2005.
- [43] Spierings AB, Herres N, Levy G. Influence of the particle size distribution on surface quality and mechanical properties in additive manufactured stainless steel parts. *Solid Free Fabr* 2011, 17: 195–202.
- [44] Tan JH, Wong WLE, Dalgarno KW. An overview of powder granulometry on feedstock and part performance in the selective laser melting process. *Addit Manuf* 2017, 18: 228–255.
- [45] Teodorescu M, Bercea M. Poly(vinylpyrrolidone) – A Versatile Polymer for Biomedical and Beyond Medical Applications. *Polym – Plast Technol Eng* 2015, 54: 923–943.
- [46] Fernandes TJ, Mavropoulos E, Campos GB, et al. PVP Addition during Hydroxyapatite Synthesis: Effect on Albumin Adsorption. *Key Eng Mater* 2011, 493–494: 757–762.

- [47] Zhou P, Qi H, Zhu Z, et al. Development of SiC/PVB Composite Powders for Selective Laser Sintering Additive Manufacturing of SiC. *Materials (Basel)* 2018, 11: 2012.
- [48] Hayama M, Yamamoto KI, Kohori F, et al. Nanoscopic behavior of polyvinylpyrrolidone particles on polysulfone/polyvinylpyrrolidone film. *Biomaterials* 2004, 25: 1019–1028.
- [49] Liu J. BINDER COMPOSITION. U.S. patent 0189405, Dec. 2002.
- [50] Xue W, Bandyopadhyay A, Bose S. Polycaprolactone coated porous tricalcium phosphate scaffolds for controlled release of protein for tissue engineering. *J Biomed Mater Res - Part B Appl Biomater* 2009, 91: 831–838.
- [51] Wei Q, Wang Y, Li X, et al. Study the bonding mechanism of binders on hydroxyapatite surface and mechanical properties for 3DP fabrication bone scaffolds. *J Mech Behav Biomed Mater* 2016, 57: 190–200.
- [52] Jacob G, Brown CU, Donmez MA. The influence of spreading metal powders with different particle size distributions on the powder bed density in laser-based powder bed fusion processes. *Natl Inst Stand Technol* 2018.
- [53] Zhao X, Yim CH, Du N, et al. Crosslinked Chitosan Networks as Binders for Silicon/Graphite Composite Electrodes in Li-Ion Batteries. *J Electrochem Soc* 2018, 165: A1110–A1121.
- [54] Okada T, Nobunaga Y, Konishi T, et al. Preparation of chitosan-hydroxyapatite composite mono-fiber using coagulation method and their mechanical properties. *Carbohydr Polym* 2014, 175: 355–360.
- [55] Chavanne P, Stevanovic S, Wüthrich A, et al. 3D printed chitosan / hydroxyapatite scaffolds for potential use in regenerative medicine. *Biomed Tech* 2013, 58.

Figures

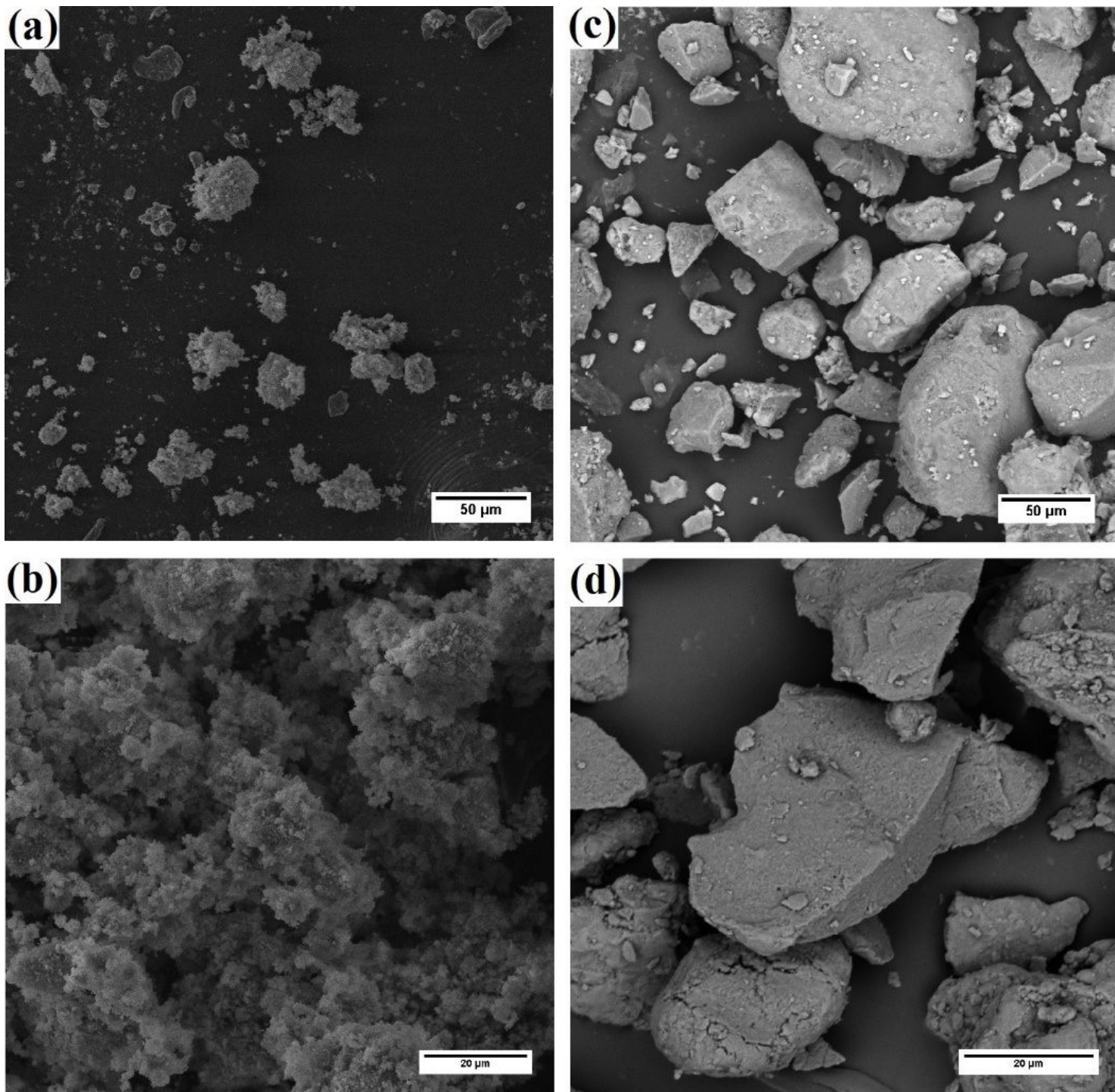


Figure 1

EM images of (a), (b) Hydroxyapatite powder, (c), (d) Ceramic/polymer composite powder

A5

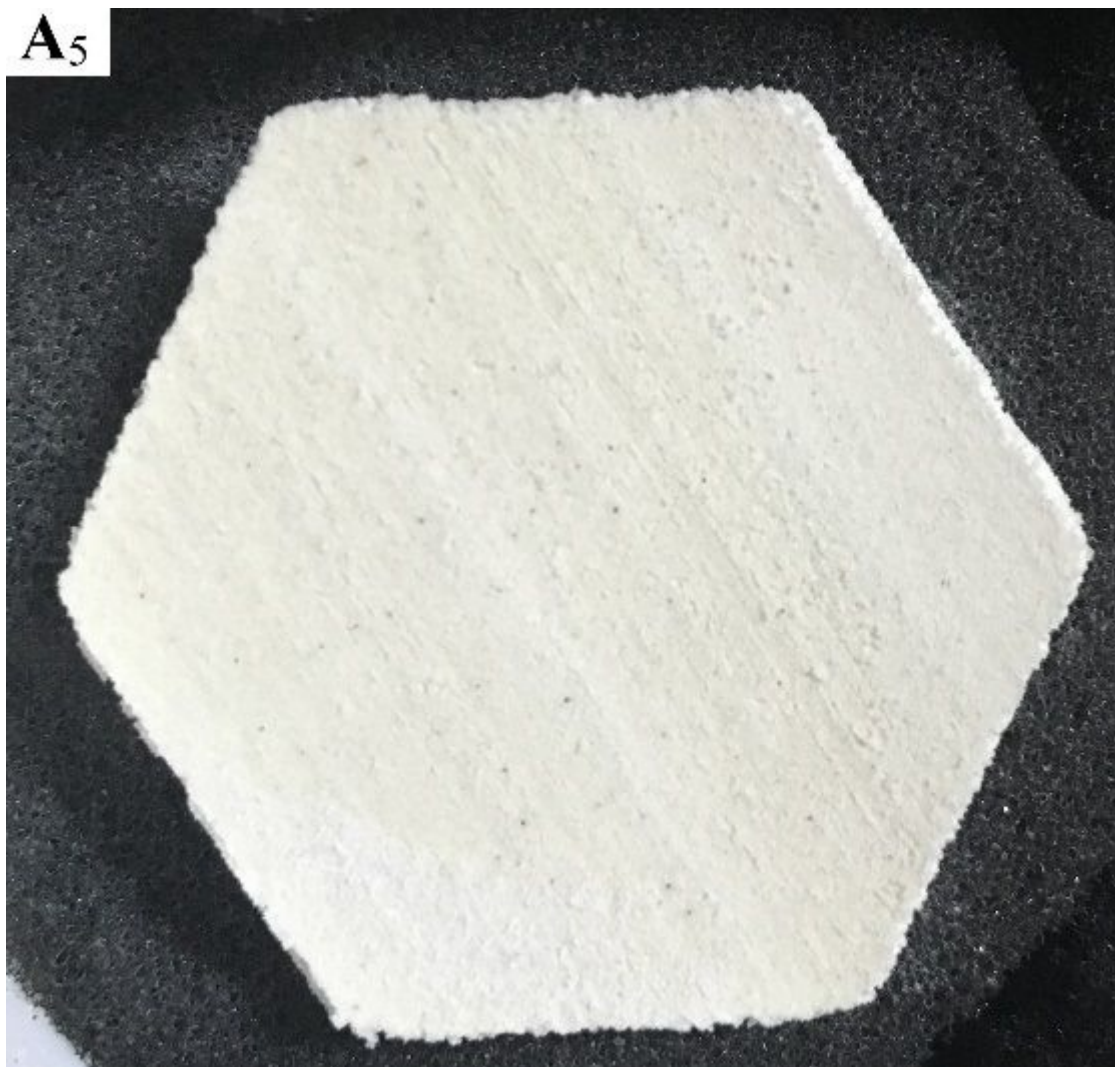


Figure 2

3D printed sample of A5 sample

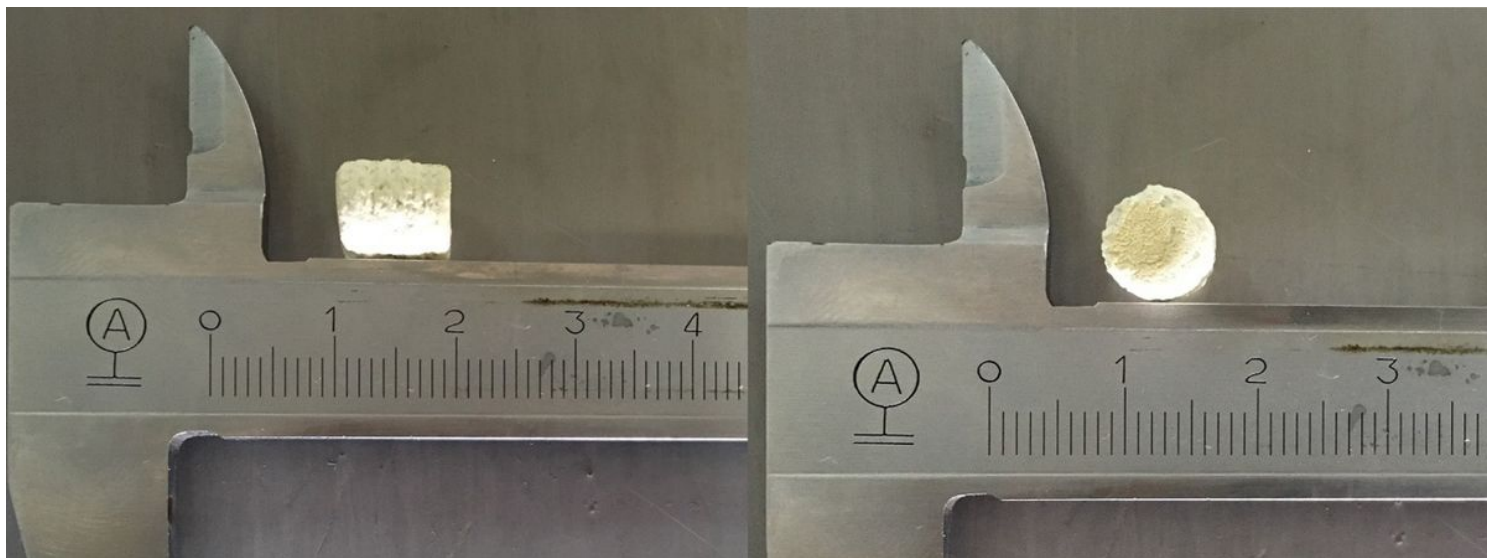


Figure 3

The printed sample with height to diameter ratio of 1 to 0.5

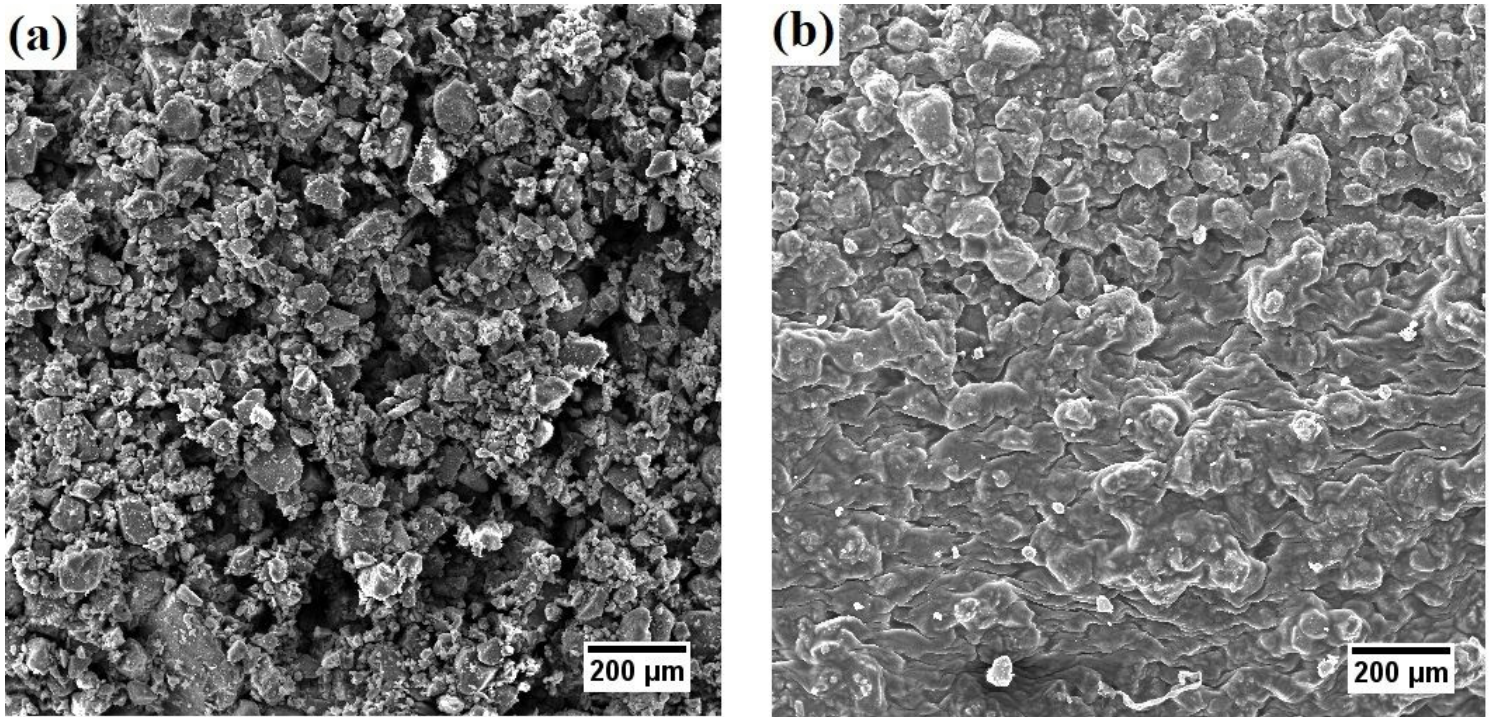


Figure 4

Scanning electron microscope images of a) A5 before flash dipping in Chitosan solution and b) A5-D after flash dipping in Chitosan solution.

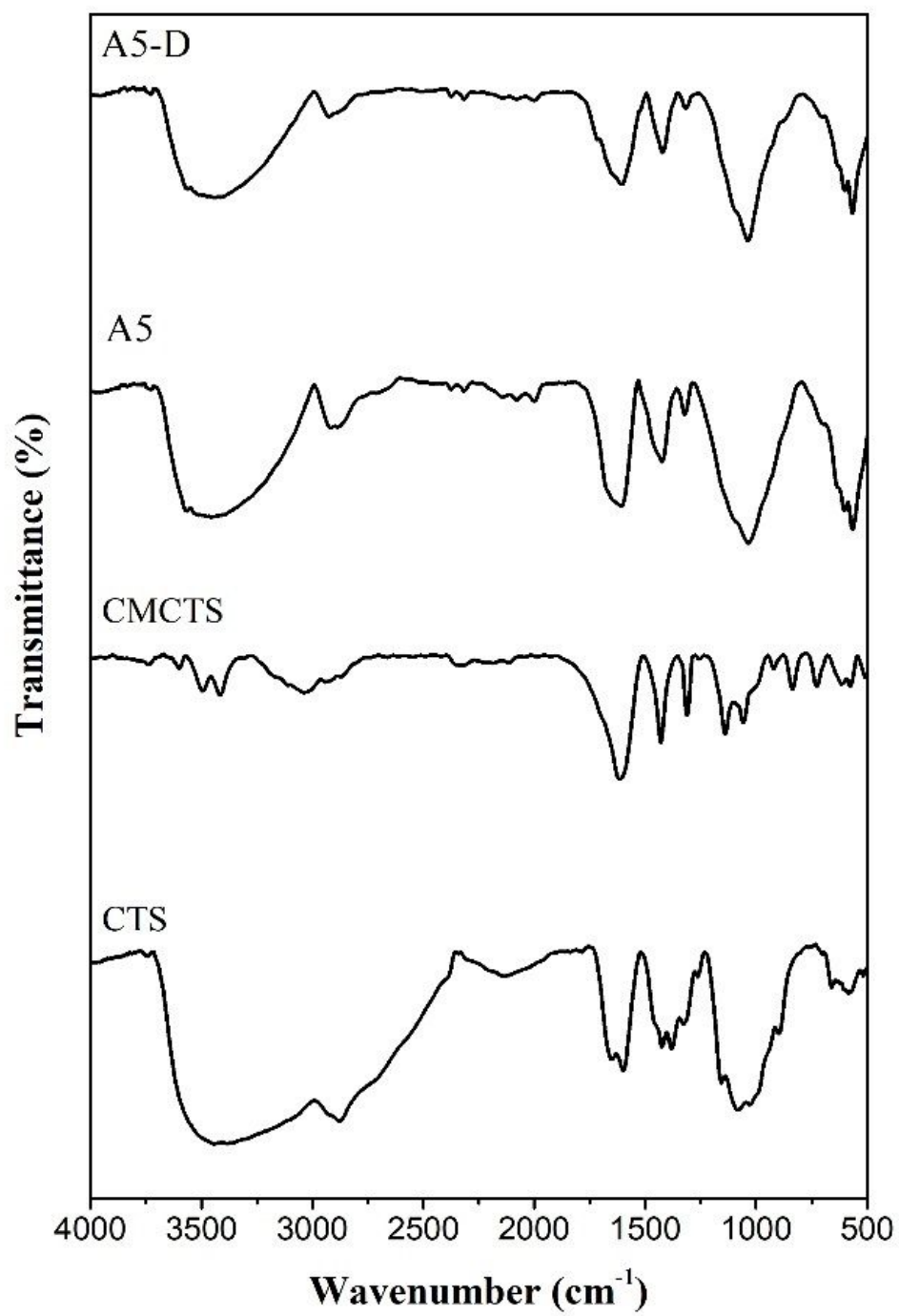


Figure 5

FTIR spectra of CTS, CMCTS, A5 and A5-D Composite Samples

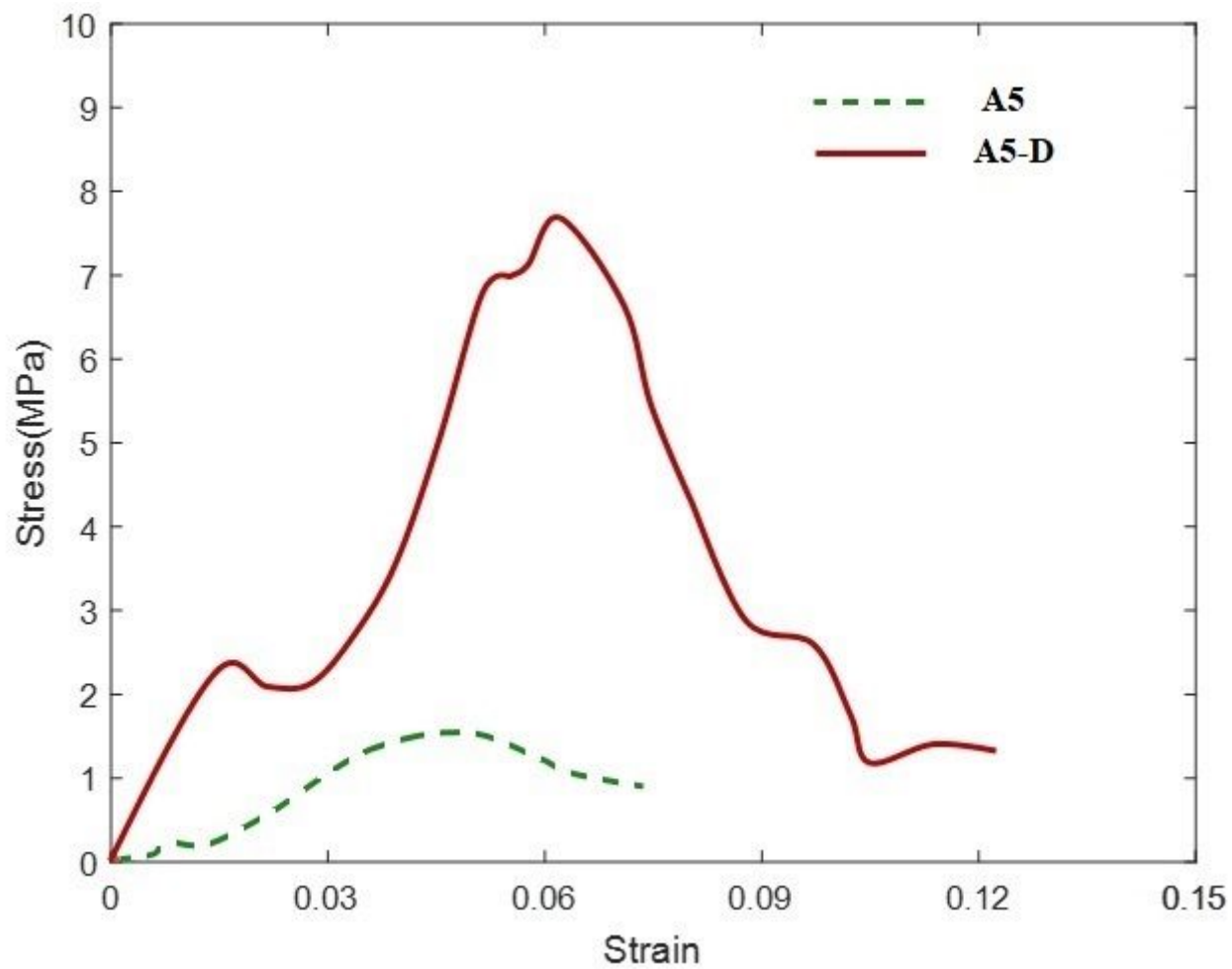


Figure 6

Stress-strain curves of A5 and A5-D samples